JOURNAL OF SYNCHROTRON RADIATION
ISSN 1600-5775

Evolution of the magnetic hyperfine field profiles in an ion-irradiated $Fe_{60}Al_{40}$ film measured by nuclear resonant reflectivity

Marina Andreeva,[a]* Alevtina Smekhova,[b,c] Roman Baulin,[a,d] Yurii Repchenko,[d] Rantej Bali,[e] Carolin Schmitz-Antoniak,[f] Heiko Wende,[g] Ilya Sergueev,[h] Kai Schlage[h] and Hans-Christian Wille[h]

[a]Faculty of Physics, M. V. Lomonosov Moscow State University, Moscow 119991, Russian Federation, [b]Peter Grünberg Institute (PGI-6), Jülich Research Center, 52425 Jülich, Germany, [c]Helmholtz-Zentrum Berlin für Materialien und Energie (HZB), 12489 Berlin, Germany, [d]National Research Centre 'Kurchatov Institute', Pl. Kurchatova 1, Moscow 123182, Russian Federation, [e]Helmholtz-Zentrum Dresden-Rossendorf, Bautzner Landstraße 400, 01328 Dresden, Germany, [f]Technical University of Applied Sciences Wildau, 15745 Wildau, Germany, [g]Faculty of Physics and Center for Nanointegration Duisburg-Essen (CENIDE), University of Duisburg-Essen, 47048 Duisburg, Germany, and [h]Deutsches Elektronen-Synchrotron DESY, 22607 Hamburg, Germany. *Correspondence e-mail: mandreeva1@yandex.ru

Received 11 May 2021
Accepted 27 July 2021

Edited by V. Favre-Nicolin, ESRF and Université Grenoble Alpes, France

Keywords: magnetic patterning; ion irradiation; X-ray reflectivity; hyperfine interactions; nuclear resonant scattering; magnetic depth profiles; Mössbauer spectroscopy.

Nuclear resonant reflectivity (NRR) from an $Fe_{60}Al_{40}$ film was measured using synchrotron radiation at several grazing angles near the critical angle of total external reflection. Using laterally resolved measurements after irradiation with 20 keV Ne^+ ions of gradually varying fluence of 0–3.0 × 10^{14} ions cm^{-2}, the progressive creation of the ferromagnetic A2 phase with increasing ion fluence was confirmed. The observed depth selectivity of the method has been explained by application of the standing wave approach. From the time spectra of the nuclear resonant scattering in several reflection directions the depth profiles for different hyperfine fields were extracted. The results show that the highest magnetic hyperfine fields (∼18–23 T) are initially created in the central part of the film and partially at the bottom interface with the SiO_2 substrate. The evolution of the ferromagnetic onset, commencing at a fixed depth within the film and propagating towards the interfaces, has been directly observed. At higher fluence (3.0 × 10^{14} ions cm^{-2}) the depth distribution of the ferromagnetic fractions became more homogeneous across the film depth, in accordance with previous results.

1. Introduction

The ability to control magnetic properties spatially at the nanoscale can be useful for devices requiring magnetic modulation, such as data storage media. Modulation of the saturation magnetization can be achieved in selected materials where atomic displacements lead to drastic changes in magnetic behaviour. A prototype material is the $Fe_{60}Al_{40}$ alloy, which is known to be paramagnetic in its B2 ordered state (Huffman & Fisher, 1967; Beck, 1971). Disorder caused by site swapping between the Fe and Al atoms invokes an increase in the Fe–Fe nearest-neighbour interaction along with an increase in the lattice parameter, leading to the onset of ferromagnetism. The disordered $Fe_{60}Al_{40}$ phase is of the A2 structure, and this B2 to A2 transition can be induced by irradiation with energetic ions (Fassbender & McCord, 2008; Menéndez *et al.*, 2009; Bali *et al.*, 2014) or laser pulses (Ehrler *et al.*, 2018). Recently it has been shown that the paramagnetic to ferromagnetic phase transformation can also be reversible in other similar alloys such as B2 $Fe_{50}Rh_{50}$ (Merkel *et al.*,

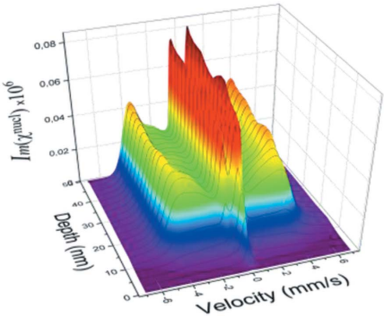

2020). Thus, magnetic properties can be modulated in alloy thin films by modification of lattice disorder, realized with industrially relevant ion accelerators.

In the case of ion irradiation, energetic ions penetrate into the B2 $Fe_{60}Al_{40}$ structure, generating vacancies that recombine with thermally diffusing atoms. Since the recombination process is stochastic, site swapping between the Fe and Al atoms occurs. The antisite defects thus formed are correlated with the ferromagnetic onset (Ehrler *et al.*, 2020). Since the depth penetration of ions in matter follows a quasi-Gaussian profile, and the penetration depth can be controlled via the ion energy, it is possible to exert a degree of control on the depth distribution of the magnetization (Röder *et al.*, 2015).

Irradiation of B2 $Fe_{60}Al_{40}$ thin films with light noble-gas ions, such as Ne^+, has been deployed to manipulate magnetic domains (Tahir *et al.*, 2015*b*). The investigation was performed using the longitudinal magneto-optical Kerr effect (L-MOKE) with magnetic domain imaging. The dynamic behaviour of the Ne^+-irradiated $Fe_{60}Al_{40}$ thin films has been investigated by ferromagnetic resonance (Tahir *et al.*, 2015*a*; Schneider *et al.*, 2019). It has been shown that the observed spin wave modes are directly related to the effective ferromagnetic thickness which increases with increasing ion energy, as increasing ion energy leads to deeper penetration. Röder *et al.* (2015) investigated $Fe_{60}Al_{40}$ thin films irradiated by Ne^+ ions of different energies using electron holography in transmission electron microscopy (TEM). The depth and lateral distribution of the magnetized regions at the nanoscale were observed by magnetic flux lines which became apparent via the phase shift of the scattered electrons. By means of X-ray magnetic circular dichroism (XMCD) and analysis of extended X-ray absorption fine structure (EXAFS) measurements, performed on beamline ID12 at the European Synchrotron (ESRF), it was shown that an increase in the irradiation fluence provided a progressive rise in the Fe magnetic moment, revealing the occurrence of a change in the chemical disorder in the $Fe_{60}Al_{40}$ alloy (La Torre *et al.*, 2018). Recent XMCD results obtained with soft X-rays at the Helmholtz-Zentrum Berlin (HZB) have confirmed these findings (Smekhova *et al.*, 2021).

In preceding work the main attention was paid to the saturation magnetization of the whole film, the penetration depth of the Ne^+ ions and the corresponding effective thickness of the created ferromagnetic layer. A possible decrease in ferromagnetic order near the surface caused by oxidation has already been discussed (Röder *et al.*, 2015), but the interpretation needs independent verification. At this point, X-ray methods can provide more detailed information about the magnetic structure of irradiated films. X-ray reflectometry possesses a sub-nanometre depth resolution for electronic density shaping (Segmüller, 1973; Liu *et al.*, 2013; Macke *et al.*, 2014) and this technique, complemented with resonant scattering near absorption edges or with nuclear resonant excitation, opens a way for detailed characterization of magnetization depth profiles (see *e.g.* Ishimatsu *et al.*, 1999; Jaouen *et al.*, 2004; Gibert *et al.*, 2016; Diederich *et al.*, 2007; Schlage *et al.*, 2009; Andreeva *et al.*, 2015, 2018; Khanderao *et al.*, 2020).

In this work we have used the nuclear resonant reflectivity (NRR) technique with synchrotron radiation in order to obtain the depth distribution of hyperfine fields on ^{57}Fe nuclei in an $Fe_{60}Al_{40}$ film affected irradiated by 20 keV Ne^+ ions with different fluences from 0 to 3.0×10^{14} ions cm^{-2} varying gradually along the film surface. In this way, we track the gradual increase in saturation magnetization caused by the atomic displacements. NRR can be performed for the fully ordered structure at a fluence of 0 all the way through to the disordered structure for the highest fluence considered in this study. Consequently, a detailed depth-resolved picture of magnetic phase formation has been obtained under the sequentially increasing irradiation fluence.

2. Experimental

An $Fe_{60}Al_{40}$ thin film of ~40 nm thickness was prepared by magnetron sputtering on an SiO_2(150 nm)/Si(001) substrate with further annealing in a vacuum at 773 K for 1 h to obtain the B2 ordered structure. B2 ordering is indicated by the occurrence of the 100 superstructure reflections (Bali *et al.*, 2014; Ehrler *et al.*, 2020; Smekhova *et al.*, 2021). For the present experiment the sample had a size of ~5 mm × 10 mm. 20 keV Ne^+ irradiation was undertaken with a gradually increasing fluence from 0 to 3.0×10^{14} ions cm^{-2} along the sample surface with the help of a shutter *in situ* moved in steps of ~0.1 mm (30 steps in total). In such a way a 'disorder gradient' sample was made (Fig. 1). It should be noted that the sample was not enriched by ^{57}Fe [the natural abundance is 2.14 (1)%], so preliminary NRR measurements had to be done which proved the possibility of NRR measurements with such $Fe_{60}Al_{40}$ films.

The measurements were done on the Dynamics beamline P01 at PETRA III, DESY (Deutsches Elektronen-Synchro-

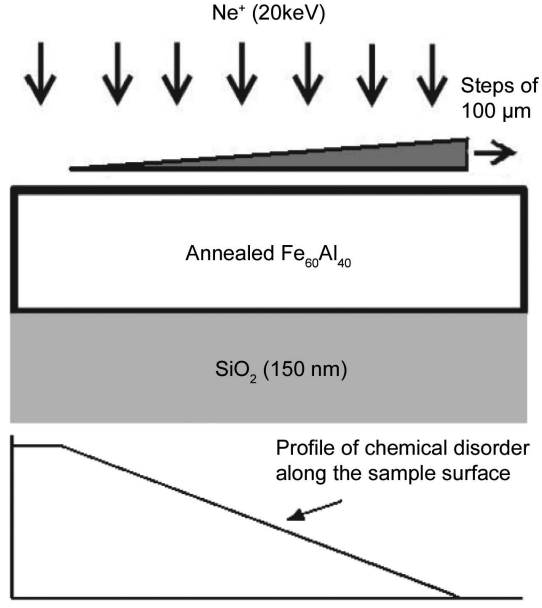

Figure 1
A schematic diagram of the sample studied.

tron, Hamburg), using nuclear resonant scattering at the 14.4 keV ^{57}Fe Mössbauer transition. During measurements, the synchrotron was operated in the 40 bunch mode with a bunch separation of 192 ns. The transverse size of the beam on the sample surface was only ∼0.16 mm which allowed laterally selected measurements. In spite of the natural abundance of ^{57}Fe (2.14%) in the sample, it was possible to measure NRR time spectra at several grazing angles in the vicinity of the critical angle with reasonable statistics. All measurements were performed at room temperature.

Nuclear resonant (Mössbauer) scattering with synchrotron radiation on the P01 beamline is basically measured in the time domain by detecting the delayed response after the prompt pulse of the synchrotron beam. This is possible due to the relatively long lifetime of the excited resonant level (141 ns for the ^{57}Fe isotope). In contrast to ordinary Mössbauer spectroscopy, the hyperfine splitting of the nuclear levels appears in the time evolution of the delayed response as quantum beats (see *e.g.* Trammell & Hannon, 1978; Rüffer *et al.*, 1991; Smirnov, 1999). The period of oscillations Δt is connected to the energy difference of the interfering resonant lines ΔE by the simple expression $\Delta E = h/\Delta t$ (h is the Planck constant). The rather fast oscillations in the NRR time spectra are direct evidence of the appearance of magnetic ordering. The X-ray reflectivity was measured before the NRR measurements as the prompt response to the SR pulse.

3. Results and discussion

X-ray reflectivity curves were measured for the resonant wavelength of 0.086 nm at different positions of the sample (Fig. 2). Each curve contains ∼19 Kiessig fringes in the angular range from 0 to 0.021 rad, directly determining the film thickness (Segmüller, 1973).

A very small increase in the film thickness (∼0.5 nm) due to the irradiation is revealed by the change in the oscillation frequency. The result corresponds to the ∼1% increase in the lattice parameter determined by X-ray diffraction (Liedke *et al.*, 2015; Ehrler *et al.*, 2020; La Torre *et al.*, 2018). The peculiarities of the oscillation shapes characterize the top and bottom interfaces. The fairly good fit of their notable variations indicates a tiny change in the top defective layer of ∼10 nm thickness with different irradiation fluences (Fig. 3). The defect-containing thickness includes the surface oxide layer.

The NRR time spectra were measured at several grazing angles near the critical angle of total external reflection. The external field B^{ext} of 0.13 T was applied parallel or perpendicular to the synchrotron beam in the surface plane. This value was chosen to be high enough to magnetize the sample fully and arrange magnetic hyperfine fields along the external field. Magnetically split resonant spectra with relatively large ΔE give a recognizable fast oscillation pattern in the NRR time spectra, therefore the appearance of quantum beat oscillations indicates the progressive creation of the ferromagnetic A2 phase in the $Fe_{60}Al_{40}$ film with increasing ion fluence (Fig. 4).

The treatment of the NRR time spectra was performed on the basis of the matrix theory of reflectivity from anisotropic multilayers (Borzdov *et al.*, 1976; Azzam & Bashara, 1977). In this theory the propagation of radiation in the reflecting stratified media is described by a 4×4 propagation matrix, characterizing the evolution of the four tangential components

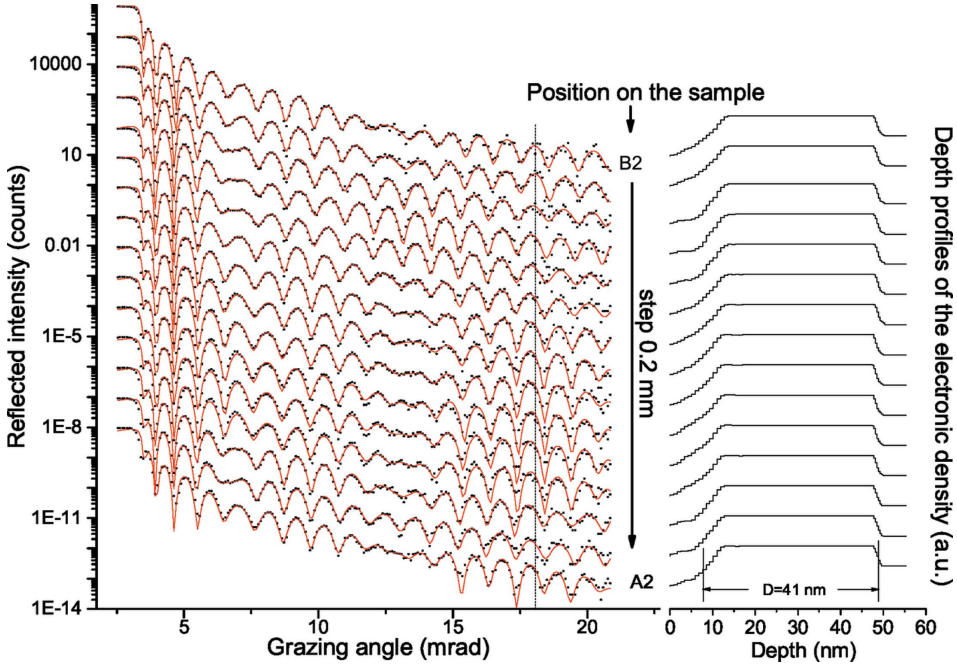

Figure 2
X-ray reflectivity curves for 14.4 keV radiation measured at 15 different positions on the gradient $Fe_{60}Al_{40}$ film (left-hand side, dots are the experimental data and solid lines are the fit) and the results of their fit (right-hand side), giving the depth profiles of the X-ray refraction $|\delta|$ proportional to the electronic density. All curves are shifted vertically. The dashed vertical line is drawn in order to clarify the small change in the oscillation frequency, corresponding to the increase in the film thickness caused by ion irradiation.

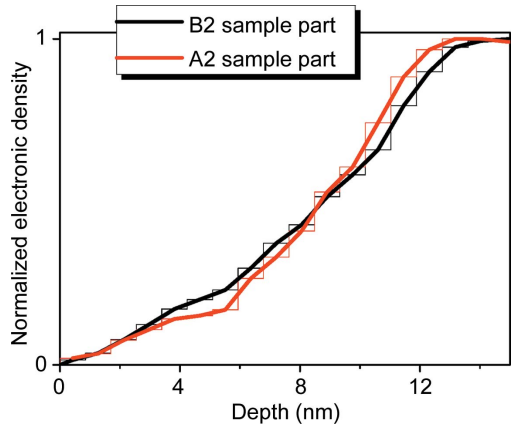

Figure 3
The scaled-up part of the electronic density for two ends of the film, obtained from X-ray reflectivity curves, demonstrating the change in the top defective layer under ion irradiation.

of the electric and magnetic fields of radiation $\{H_x(z), H_y(z), -E_y(z), E_x(z)\}$ along depth z. In the case of grazing angles θ the propagation matrix is represented by the expression (Andreeva & Rosete, 1986*a*,*b*; Irkaev *et al.*, 1973)

$$\hat{M} \simeq \begin{pmatrix} 0 & 0 & 1 & 0 \\ \hat{\chi}_{xz} & 0 & 0 & \sin^2\theta + \hat{\chi}_{xx} \\ \sin^2\theta + \hat{\chi}_{zz} & 0 & 0 & \hat{\chi}_{zx} \\ 0 & 1 & 0 & 0 \end{pmatrix}. \quad (1)$$

The susceptibility tensor $\hat{\chi}$ of the Mössbauer medium consists of two parts associated with the scattering by electrons $\chi^{\rm el}$ and by resonant nuclei $\hat{\chi}^{\rm nucl}(\omega)$,

$$\hat{\chi} = \chi^{\rm el} + \hat{\chi}^{\rm nucl}(\omega). \quad (2)$$

The electronic part of the susceptibility is a scalar function of z (apart from the absorption edges),

$$\chi^{\rm el}(z) = -\frac{\lambda^2}{\pi}\,\rho(z)\,r_0(Z + \Delta f' - i\Delta f''), \quad (3)$$

where $\rho(z)$ is the volume density of atoms, r_0 is the classical electron radius, Z is the atomic number, and $\Delta f'$ and $\Delta f''$ are the anomalous dispersion corrections for the scattering amplitude. It does not depend on the energy in the very narrow frequency range of Mössbauer scattering, though it essentially influences the Mössbauer reflectivity spectra in the energy and time domains. Therefore, the fit of the X-ray reflectivity curve for each beam position was done before fitting the corresponding NRR time spectra.

The nuclear part of the susceptibility $\hat{\chi}^{\rm nucl}(\omega, z)$ is represented by the expression (Trammell, 1962; supplement to Andreeva *et al.*, 2015)

$$\hat{\chi}^{\rm nucl}(\omega, z) = -A^{\alpha{\rm Fe}} \sum_j C_j(z) \sum_{m_{\rm e}, m_{\rm g}} \frac{\left|\langle I_{\rm g} m_{\rm g} L \Delta m | I_{\rm e} m_{\rm e}\rangle\right|^2}{\hbar\omega - E_{jR}(m_{\rm e}, m_{\rm g}) + (i\Gamma_j/2)} \hat{\mathbf{h}}_{\Delta m,j} \cdot \hat{\mathbf{h}}^*_{\Delta m,j}, \quad (4)$$

where $m_{\rm e}$ and $m_{\rm g}$ are the magnetic quantum numbers of the excited and ground levels, respectively, j numerates the kind of hyperfine field (multiplet number in a Mössbauer spectrum), $E_{jR}(m_{\rm e}, m_{\rm g})$ are the hyperfine transition energies, which are determined for each multiplet by common Mössbauer para-

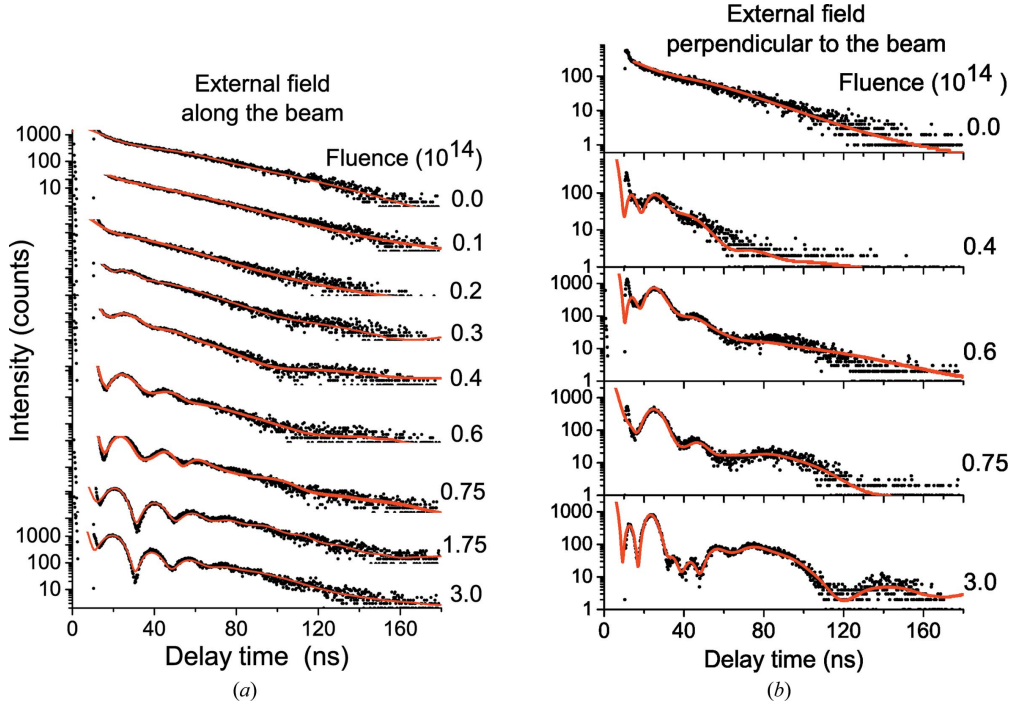

Figure 4
NRR time spectra measured at the critical angle of total external reflection and at different positions of the synchrotron beam on the gradually irradiated sample. The external magnetic field $B^{\rm ext}$ was applied either (*a*) parallel to the synchrotron beam direction or (*b*) perpendicular to it. Symbols are the experimental counts and lines are the fit.

meters such as the isomer shift δ_j (or central shift CS), magnetic hyperfine field B_j^{hf} and quadrupole splitting ΔE_j^Q, Γ_j is the full width of resonant level j, $\langle I_g m_g L \Delta m | I_e m_e \rangle$ are the Clebsch–Gordan coefficients, and $\hat{\boldsymbol{h}}_{\Delta m,j}$ in equation (4) are the spherical unit vectors (orts) of the hyperfine field principal axis, $\Delta m = m_e - m_g = \pm 1, 0$ for the M1 transition. The outer product of these unit vectors $\mathbf{h}_{\Delta m} \cdot \mathbf{h}^*_{\Delta m}$ determines the tensor properties of the nuclear resonance susceptibility. $A^{\alpha\mathrm{Fe}}$ is a constant which includes different parameters of the nuclear 14.4 keV transition in ^{57}Fe:

$$A^{\alpha\mathrm{Fe}} = -\frac{\lambda}{2\pi}\frac{\Gamma_{\mathrm{nat}}}{2}\sigma_{\mathrm{res}}\frac{2L+1}{2I_e+1}\rho^{\alpha\mathrm{Fe}}Q^{\mathrm{enrich}}f^{\mathrm{LM}} \simeq -7.19\times10^{-6}\,\mathrm{mm\,s^{-1}}, \quad (5)$$

where $L = 1$, $I_e = 3/2$, $I_g = 1/2$, $\sigma_{\mathrm{res}} = 2.56\times10^{-4}$ nm^2 is the resonant cross section, $\lambda = 0.086$ nm, $\Gamma_{\mathrm{nat}} = 0.097$ mm s^{-1} (4.665 neV), f^{LM} is the Lamb–Mössbauer factor which is ~0.7 in α-Fe at room temperature, $Q^{\mathrm{enrich}} = 0.95$ is the ideal ^{57}Fe isotope enrichment and $\rho^{\alpha\mathrm{Fe}} = 84.9$ nm^{-3} is the volume density of the iron atoms in α-Fe. In our case $Q^{\mathrm{enrich}} = 0.0214$ and the volume density of iron atoms in $Fe_{60}Al_{40}$ differs from the density in α-Fe. This essentially decreases $\hat{\chi}^{\mathrm{nucl}}$. In calculations the real parameters of the nuclear resonant scattering are taken into account by a proper normalization of the coefficients $C_j(z)$.

The dimensionless coefficients $C_j(z)$ in equation (4) are the 'weight' of the jth multiplet in the total susceptibility, which takes into account the relative volume density of the resonant nuclei possessing j types of hyperfine splitting, the given ^{57}Fe enrichment and the possible difference of f_j^{LM} from the accepted value of 0.7 due to a different environment or temperature. Fitting the depth profiles $C_j(z)$ is a basic task for the interpretation of NRR spectra, along with determinations of the Mössbauer parameters B_j^{hf}, ΔE_j^Q and δ_j, and the orientation of $\hat{\boldsymbol{h}}_{\Delta m,j}$ at each position of the gradient sample. For the model calculations and for a fit of the experimental NRR spectra the program pack *REFTIM* has been used (Andreeva, 2008). The fitting results for the NRR time spectra measured at several grazing angles in the vicinity of the critical angle are presented in Fig. 5.

The difficulty of the fit was connected to the rather smeared hyperfine field distribution, typical for disordered FeAl alloys (Yelsukov *et al.*, 1992; Voronina *et al.*, 2018), at each depth. This distribution was approximated by four multiplets specific to each position on the sample, excluding the case of the unirradiated part of the sample (top row in Fig. 5) where just two resonant singlets were sufficient for an acceptable fit. During the fit their depth distribution in 38 steps across the film thickness was obtained. The shape of the total density of ^{57}Fe nuclei was fixed to the depth profile of the electronic density (dashed lines above the partial depth profiles for nuclei with selected types of hyperfine fields in the middle column of Fig. 5). The maximum of this total depth profile was normalized to the expected density of ^{57}Fe atoms in the $Fe_{60}Al_{40}$ structure, taking into account the natural abundance of the ^{57}Fe isotope. Due to the obtained depth profile for each multiplet (middle column in Fig. 5), their sum gives the total resonant spectrum, characterizing the magnetic hyperfine splitting at each depth (right-hand column in Fig. 5).

The fitting results demonstrate that the relative weight of the magnetically split resonant contributions increases with increasing irradiation fluence. These findings are in agreement with the results obtained from XMCD measurements at the Fe K edge (La Torre *et al.*, 2018) and from soft X-ray studies (Smekhova *et al.*, 2021).

The essential advantage of the present NRR experiment is that it exposes the depth distribution of different magnetic and paramagnetic fractions inside the irradiated film and their redistribution under increasing irradiation fluence. As follows from Fig. 5, in the initial stages of irradiation the ferromagnetic part, giving the mostly split resonant lines (corresponding to magnetic hyperfine fields of ~18–23 T), appeared not at the surface but in the central part of the film (second and third rows in Fig. 5). This result obviously follows from the change in NRR time spectra with varying angle. At angles lower than the critical one, where the penetration depth for the incident radiation is comparable with the thin surface layer, the 'magnetic' oscillations are less pronounced than at the critical angle, where the penetration depth essentially increases.

Calculations performed on the basis of the binary collision approximation with the *TRIM* program (Ziegler *et al.*, 2010) have also shown that the maximum of the DPA (displacements per atom) depth distribution (Bali *et al.*, 2014) occurs at a certain depth below the surface. It is supposed that atomic displacements produced by collisions leave a cascade of vacancies and interstitial atoms, as well as more complex clusters of defects, and the created disorder is directly connected to the magnetization. According to Huffman & Fisher (1967), the region of moment-bearing atoms has to be large enough to behave ferromagnetically at room temperature, and preferably within the film volume. The formation of magnetic inhomogeneities obviously follows from the rather broad hyperfine field distribution at each depth. Their morphology cannot be studied by NRR, but other methods can be used like nuclear or X-ray resonant grazing-incidence small-angle X-ray scattering (GISAXS) (Erb *et al.*, 2017; Ragulskaya *et al.*, 2019).

The fitting also shows that ferromagnetic fractions are partially formed at the interface with the SiO_2 substrate (probably due to the imperfections presented near this interface). Some ferromagnetic regions appear to be present at the interfacial region. This may occur due to interfacial inhomogeneities or uncertainties in the analysis, which will be discussed later.

At higher fluence (3.0×10^{14} ions cm^{-2}) the depth distribution of the ferromagnetic fractions becomes more homogeneous across the film depth (bottom row in Fig. 5). This is seen better in Fig. 6, where the average $B_{\mathrm{Av}}^{hf}(z)$ is presented for three different levels of fluence, corresponding to Fig. 5. This result more or less coincides with the direct holographic observations in TEM through the measured gradient of the

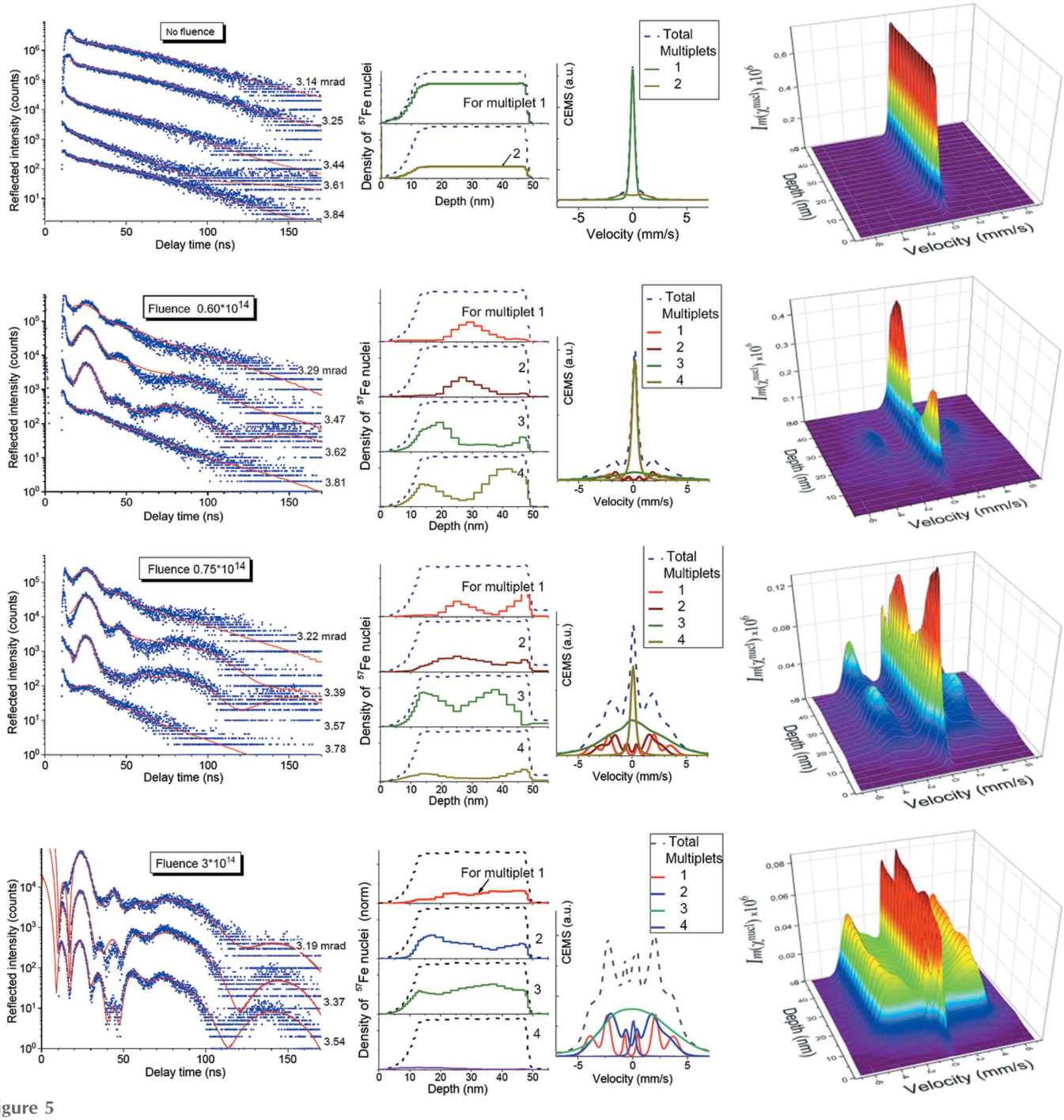

Figure 5
(Left) NRR time spectra measured at several grazing angles in the vicinity of the critical one for selected positions on the $Fe_{60}Al_{40}$ gradient sample (symbols are the experimental counts and lines are the fit). (Middle) The depth distribution of the ^{57}Fe nuclei with selected types of hyperfine interaction and the corresponding resonant spectra for the normal direction of the radiation obtained by the fit. (Right) Overall resonant spectra at each depth $\mathrm{Im}[\chi^{\mathrm{nucl}}(\omega, z)]$ calculated for the direction along the grazing-incidence synchrotron beam.

magnetic phase shift (Röder *et al.*, 2015) which shows a practically flat magnetization distribution in an $Fe_{60}Al_{40}$ film after Ne^+-ion irradiation with even higher fluence (6.0×10^{14} ions cm^{-2}).

The detection of ferromagnetic fractions at the interface with the SiO_2 substrate is not fully reliable due to the restricted sensitivity of the radiation to that deep part of the film at the grazing angles used here. It can be shown that the maximum sensitivity of the method is determined by the radiation field amplitude inside the sample. The nuclear resonant scattering in the studied $Fe_{60}Al_{40}$ film is essentially smaller than the electronic scattering because the sample is not enriched by ^{57}Fe. In such a case the NRR amplitude can be described by the generalized kinematic approximation (Andreeva *et al.*, 2019). Assuming σ polarization of the synchrotron beam, the frequency-dependent part of the

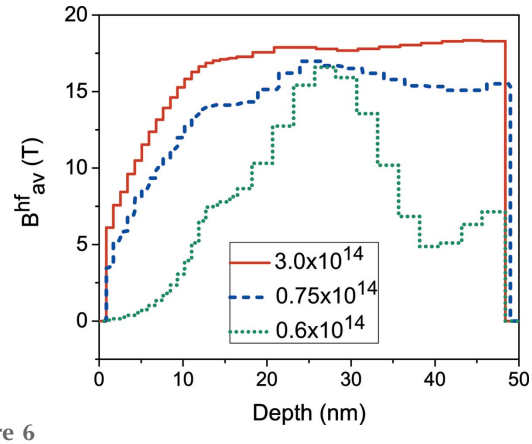

Figure 6
The depth dependence of the average magnetic hyperfine field obtained from the fitting results shown in Fig. 5 for three different irradiation fluences.

reflectivity amplitude can be calculated in this approach by the expression

$$R^{\sigma\to\sigma',\sigma\to\pi'}(\theta,\omega) = \frac{\pi}{\lambda\sin\theta}\int \chi^{\mathrm{nucl},\sigma\to\sigma',\sigma\to\pi'}(z,\omega)\,E_\sigma^2(\theta,z,\omega)\,\mathrm{d}z, \qquad (6)$$

which after Fourier transform gives the NRR time spectra,

$$I(\theta,t) = \left|\frac{1}{2\pi}\int_{-\infty}^{\infty} R^{\sigma\to\sigma'}(\theta,\omega)\exp(-i\omega t)\,\mathrm{d}\omega\right|^2 + \left|\frac{1}{2\pi}\int_{-\infty}^{\infty} R^{\sigma\to\pi'}(\theta,\omega)\exp(-i\omega t)\,\mathrm{d}\omega\right|^2. \qquad (7)$$

If the nuclear resonant scattering is small enough compared with the scattering by electrons, the calculation of $E_\sigma(\theta,z)$ can be done neglecting the nuclear resonance scattering, in other words taking into account only $\chi^{\mathrm{el}}(z)$ and applying the simple Parratt algorithm (Parratt, 1954). Thereafter it is supposed that the $E_\sigma(\theta,z)$ distribution inside the sample will be applicable over all of the resonant interaction energy region.

The calculated 'squared standing wave' distribution $|E_\sigma^2(\theta,z)|^2$ inside the sample as a function of the grazing-incidence angle is presented in Fig. 7(*b*). According to equation (6) it determines the shape of the NRR angular curve [Fig. 7(*a*)] measured as an integral over the delayed (after prompting by the synchrotron radiation excitation) reflectivity:

$$I^{\mathrm{NRR}}(\theta) = \int_{\varepsilon}^{T} I(\theta,t)\,\mathrm{d}t. \qquad (8)$$

Here, T is the interval between synchrotron pulses and ε is the small delay excluding the prompting pulse influence.

The NRR angular curve is not similar to an X-ray reflectivity curve (Baron *et al.*, 1994) as it has a sharp maximum at the critical angle. The origin of this peak has been explained by the standing wave influence created by the prompt electronic scattering (Andreeva & Lindgren, 2002, 2005). The

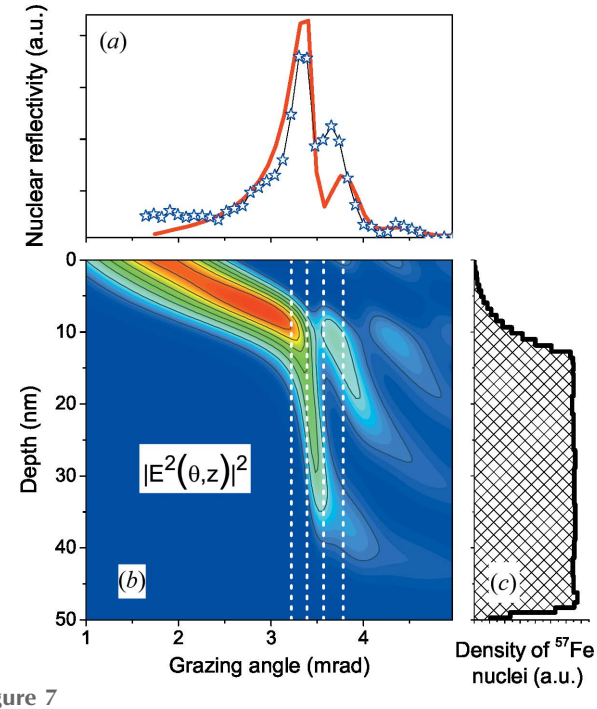

Figure 7
(*a*) The integrated NRR angular curve $I^{\mathrm{NRR}}(\theta)$ for measured data (symbols) and calculated using equations (6)–(8) (solid line). (*b*) The angular depth distribution of $|E_\sigma^2(\theta,z)|^2$. (*c*) The depth distribution of the ^{57}Fe nuclei. Calculations were done for the part of the $Fe_{60}Al_{40}$ sample irradiated with a fluence of 0.75×10^{14} ions cm^{-2} (third row in Fig. 5). The function $|E_\sigma^2(\theta,z)|^2$ in panel (*b*) is normalized to the amplitude of the incident wave $E_0 = 1$ and the colour gradient changes from 0 to 16. The vertical dashed lines in (*b*) mark the angles at which the NRR time spectra (Fig. 5, left-hand column) were measured.

standing wave picture in Fig. 7(*b*) also explains why the magnetic quantum beat oscillations on the time spectra are more pronounced at a grazing angle of 3.57 mrad than at 3.78 mrad. The maximum value of $|E_\sigma^2(\theta,z)|^2$ for the last dashed line at 3.78 mrad in Fig. 7(*b*) compared with the dashed line at 3.57 mrad is shifted to the surface where the created magnetization is smaller according to our calculations (depth profiles of magnetically split spectra in the last column of Fig. 5). The amplitude of $|E_\sigma^2(\theta,z)|^2$ near the substrate at the grazing angles used here is quite small and therefore the nuclear resonant contribution to the total reflectivity from the bottom region of the film is not so essential. Thus, for more reliable results on the magnetization near the $Fe_{60}Al_{40}/SiO_2$ interface, measurements of the NRR time spectra should be done at larger grazing angles. However, the NRR intensity has a maximum near the critical angle and drops rapidly with increasing angle. Therefore, measurements at larger angles are difficult, especially for our non-enriched sample.

The comparison of calculations of the NRR spectra in the energy and time domains by the exact and approximate algorithms shown in Fig. 8 demonstrates that the approach of equations (6) and (7) is qualitatively acceptable for an evaluation of the sensitivity of the method. As long as the influence of the standing waves on the NRR spectra is proved it should be noted that calculations of the angular depth distribution of the radiation field inside a film as shown

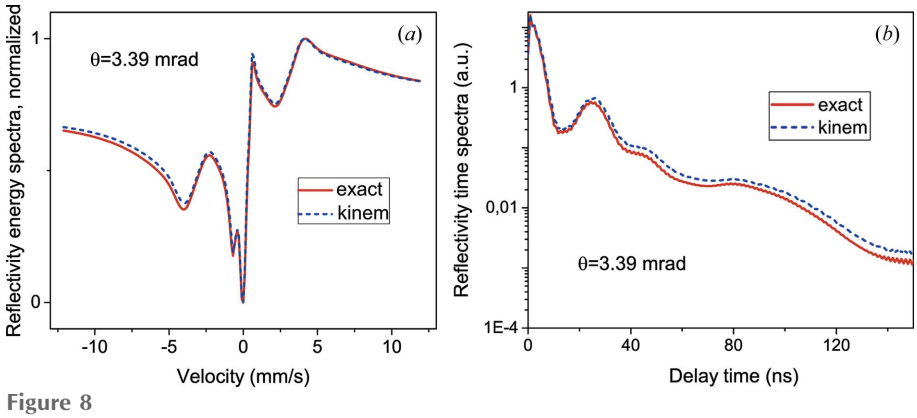

Figure 8
NRR spectra in (*a*) the energy domain and (*b*) the time domain, calculated at the critical angle of the total reflection for the same sample parameters as in Figs. 5 and 7 by the exact matrix formalism and equations (6) and (7). The very small difference in the results confirms the validity of the generalized kinematic approximation, even in the region of total reflection, and the correctness of the depth selectivity interpretation for the used method.

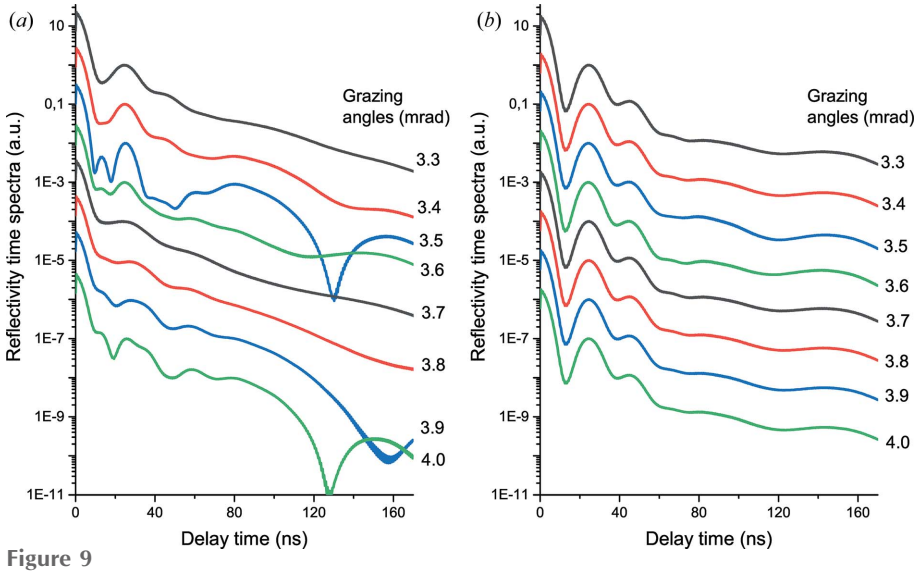

Figure 9
NRR time spectra calculated for several grazing angles for two models of hyperfine field depth distribution: (*a*) for the model obtained by fitting of the experimental data at the position irradiated with a fluence of 0.75×10^{14} ions cm^{-2} and (*b*) for the same case but with homogeneously distributed hyperfine fields across the film depth.

in Fig. 7(*b*) are desirable before an experiment, because they help to determine the right choice of angles for NRR spectrum measurements in order to get a real scan of the required properties across the film depth. An example of such an investigation was recently presented by Khanderao *et al.* (2020).

In order to exclude the possibility that the peculiar shape of the experimental NRR time spectra has originated from specific features of the reflectivity signal formation and not from the inhomogeneous depth distribution of the hyperfine fields, the NRR time spectra at several grazing angles for the case of a homogeneous depth distribution were calculated as well. For a homogeneous depth distribution no essential variations in the NRR time spectra appear. It is easy to see that the remarkable change in the oscillation shapes in Fig. 9(*a*) correlates with the brightness of the squared standing waves [Fig. 7(*b*)] in the central part of the film, where the magnetic hyperfine fields have the maximum value assumed in the model used (Fig. 5, third row).

The fast variations in $|E_\sigma^2(\theta, z)|^2$, clearly observable in Fig. 7(*b*), and the dramatic variations in the NRR time spectra with very small changes in the grazing angle [Fig. 9(*a*)], lead to the inference that NRR experiments need very accurate adjustment of the angles. If a zero angle is not exactly determined, information about the depth profiles of the investigated parameters cannot be extracted correctly. In addition, it is important to note that depth profile investigations need the measurement of NRR spectra at several grazing angles and not only at the critical angle (as is very often practised). The fit of just one spectrum gives a depth distribution of the hyperfine fields which definitely does not satisfy the other NRR spectra, and the obtained result would be rather far from the real model.

4. Summary and conclusions

The initial stages of ferromagnetic A2 phase formation in an $Fe_{60}Al_{40}$ film under 20 keV Ne^+ irradiation with increasing fluence have been investigated by visualizing the depth distribution of hyperfine fields in the film, thereby revealing details of the magnetization depth profiles. NRR time spectra measured at several grazing angles near the critical angle of total external reflection showed that the highest magnetic hyperfine fields (~18–23 T) are initially created in the central part of the film, and therefore formation of the ferromagnetic regions under irradiation does not start from the surface. This is consistent with the fact that a peak in the irradiation-induced atomic displacements occurs at a certain distance below the film surface. The results are important for the further development of computational approaches to modelling phase transformations caused by ion irradiation.

X-ray reflectivity curves measured at different points of the gradually irradiated film with a lateral resolution of ~0.2 mm show a small change in the film thickness (~0.5 nm) correlated with the lattice parameter increase and a tiny modification of the top surface layer. The depth selectivity of the NRR method has been analyzed by application of the standing wave approach. It should be noted that, despite the fact that the sample was not enriched in the ^{57}Fe isotope and contains ^{57}Fe

only of natural abundance, the synchrotron radiation-based measurements give NRR time spectra of rather good statistics.

Acknowledgements

The authors thank the staff of the P01 beamline at PETRA III for their help (proposal No. I-20160729). A. Smekhova acknowledges Professor Werner Keune for consultations and Dr Olaf Leupold for fruitful discussions during the beam time.

Funding information

RB and HW acknowledge funding by the Deutsche Forschungsgemeinschaft (DFG) – 322462997 (BA 5656/1-2 | WE 2623/14-2). AS and CS-A acknowledge funding from the Helmholtz Association (award No. VH-NG-1031). AS also acknowledges personal funding from the CALIPSO Plus project (grant agreement 730872 from the EU Framework Programme for Research and Innovation Horizon 2020).

References

Andreeva, M. A. (2008). *Hyperfine Interact.* **185**, 17–21.
Andreeva, M. A., Baulin, R. A., Chumakov, A. I., Rüffer, R., Smirnov, G. V., Babanov, Y. A., Devyaterikov, D. I., Milyaev, M. A., Ponomarev, D. A., Romashev, L. N. & Ustinov, V. V. (2018). *Phys. Rev. B*, **97**, 024417.
Andreeva, M. A., Baulin, R. A. & Repchenko, Yu. L. (2019). *J. Synchrotron Rad.* **26**, 483–496.
Andreeva, M. A. & Lindgren, B. (2002). *JETP Lett.* **76**, 704–706.
Andreeva, M. A. & Lindgren, B. (2005). *Phys. Rev. B*, **72**, 125422.
Andreeva, M. A. & Rosete, C. (1986*a*). *Vestn. Mosk. Univ. Fiz.* **41**(3), 57.
Andreeva, M. A. & Rosete, C. (1986*b*). *Poverkhnost*, **9**, 145.
Andreeva, M., Gupta, A., Sharma, G., Kamali, S., Okada, K. & Yoda, Y. (2015). *Phys. Rev. B*, **92**, 134403–1–12.
Azzam, R. & Bashara, N. (1977). *Ellipsometry and Polarized Light.* Amsterdam: North-Holland.
Bali, R., Wintz, S., Meutzner, F., Hübner, R., Boucher, R., Ünal, A. A., Valencia, S., Neudert, A., Potzger, K., Bauch, J., Kronast, F., Facsko, S., Lindner, J. & Fassbender, J. (2014). *Nano Lett.* **14**, 435–441.
Baron, A. Q. R., Arthur, J., Ruby, S. L., Chumakov, S. L., Smirnov, G. V. & Brown, G. S. (1994). *Phys. Rev. B*, **50**, 10354–10357.
Beck, P. A. (1971). *Metall. Mater. Trans. B*, **2**, 2015–2024.
Borzdov, G. N., Barkovskii, L. M. & Lavrukovich, V. I. (1976). *Zh. Prikl. Spektrosk.* **25**, 526.
Diederich, Th., Couet, S. & Röhlsberger, R. (2007). *Phys. Rev. B*, **76**, 054401.
Ehrler, J., He, M., Shugaev, M. V., Polushkin, N. I., Wintz, S., Liersch, V., Cornelius, S., Hübner, R., Potzger, K., Lindner, J., Fassbender, J., Ünal, A. A., Valencia, S., Kronast, F., Zhigilei, L. V. & Bali, R. (2018). *Appl. Mater. Interfaces*, **10**, 15232–15239.
Ehrler, J., Sanyal, B., Grenzer, J., Zhou, Sh., Böttger, R., Eggert, B., Wende, H., Lindner, J., Fassbender, J., Leyens, C., Potzger, K. & Bali, R. (2020). *New J. Phys.* **22**, 073004.
Erb, D., Schlage, K., Bocklage, L., Hübner, R., Merkel, D. G., Rüffer, R., Wille, H.-C. & Röhlsberger, R. (2017). *Phys. Rev. Mater.* **1**, 023001.
Fassbender, J. & McCord, J. (2008). *J. Magn. Magn. Mater.* **320**(3–4), 579–596.
Gibert, M., Viret, M., Zubko, P., Jaouen, N., Tonnerre, J.-M., Torres-Pardo, A., Catalano, S., Gloter, A., Stéphan, O. & Triscone, J.-M. (2016). *Nat. Commun.* **7**, 11227.
Huffman, G. P. & Fisher, R. M. (1967). *J. Appl. Phys.* **38**, 735–742.
Irkaev, S. M., Andreeva, M. A., Semenov, V. G., Belozerskii, G. N. & Grishin, O. V. (1993). *Nucl. Instrum. Methods Phys. Res. B*, **74**, 554–564.
Ishimatsu, N., Hashizume, H., Hamada, S., Hosoito, N., Nelson, C. T., Venkataraman, C. T., Srajer, G. & Lang, J. C. (1999). *Phys. Rev. B*, **60**, 9596–9606.
Jaouen, N., van der Laan, G., Johal, T. K., Wilhelm, F., Rogalev, A., Mylonas, S. & Ortega, S. (2004). *Phys. Rev. B*, **70**, 094417.
Khanderao, A. G., Sergueev, I., Wille, H. C. & Kumar, D. (2020). *Appl. Phys. Lett.* **116**, 101603.
La Torre, E., Smekhova, A., Schmitz-Antoniak, C., Ollefs, K., Eggert, B., Cöster, B., Walecki, D., Wilhelm, F., Rogalev, A., Lindner, J., Bali, R., Banerjee, R., Sanyal, B. & Wende, H. (2018). *Phys. Rev. B*, **98**, 024101.
Liedke, M. O., Anwand, W., Bali, R., Cornelius, S., Butterling, M., Trinh, T. T., Wagner, A., Salamon, S., Walecki, D., Smekhova, A., Wende, H. & Potzger, K. (2015). *J. Appl. Phys.* **117**, 163908.
Liu, Y., Wang, H.-H., Bian, G., Zhang, Z., Lee, S. S., Fenter, P. A., Tischler, J. Z., Hong, H. & Chiang, T.-C. (2013). *Phys. Rev. Lett.* **110**, 226103.
Macke, S., Radi, A., Hamann-Borrero, J. E., Verna, A., Bluschke, M., Brück, S., Goering, E., Sutarto, R., He, F., Cristiani, G., Wu, M., Benckiser, E., Habermeier, H.-U., Logvenov, G., Gauquelin, N., Botton, G. A., Kajdos, A. P., Stemmer, S., Sawatzky, G. A., Haverkort, M. W., Keimer, B. & Hinkov, V. (2014). *Adv. Mater.* **26**, 6554–6559.
Menéndez, E., Liedke, M. O., Fassbender, J., Gemming, T., Weber, A., Heyderman, L. J., Rao, K. V., Deevi, S. C., Suriñach, S., Baró, M. D., Sort, J. & Nogués, J. (2009). *Small*, **5**, 229–234.
Merkel, D. G., Lengyel, A., Nagy, D. L., Németh, A., Horváth, Z. E., Bogdán, C., Gracheva, M. A., Hegedűs, G., Sajti, S., Radnóczi, G. Z. & Szilágyi, E. (2020). *Sci. Rep.* **10**, 13923.
Parratt, L. G. (1954). *Phys. Rev.* **95**, 359–369.
Ragulskaya, A. V., Andreeva, M. A., Rogachev, A. V. & Yakunin, S. N. (2019). *Superlattice Microstruct.* **125**, 16–25.
Röder, F., Hlawacek, G., Wintz, S., Hübner, R., Bischoff, L., Lichte, H., Potzger, K., Lindner, J., Fassbender, J. & Bali, R. (2015). *Sci. Rep.* **5**, 16786.
Rüffer, R., Gerdau, E., Grote, M., Hollatz, R., Röhlsberger, R., Rüter, H. D. & Sturhahn, W. (1991). *Nucl. Instrum. Methods Phys. Res. A*, **303**, 495–502.
Schlage, K., Röhlsberger, R., Klein, T., Burkel, E., Strohm, C. & Rüffer, R. (2009). *New J. Phys.* **11**, 013043.
Schneider, T., Lenz, K., Semisalova, A., Gollwitzer, J., Heitler-Klevans, J., Potzger, K., Fassbender, J., Lindner, J. & Bali, R. (2019). *J. Appl. Phys.* **125**, 195302.
Segmüller, A. (1973). *Thin Solid Films*, **18**, 287–294.
Smekhova, A., Szyjka, Th., La Torre, E., Ollefs, K., Eggert, B., Cöster, B., Wilhelm, F., Bali, R., Lindner, J., Rogalev, A., Többens, D., Weschke, E., Luo, C., Chen, K., Radu, F., Schmitz-Antoniak, C. & Wende, H. (2021). In preparation.
Smirnov, G. V. (1999). *Hyperfine Interact.* **123/124**, 31–77.
Tahir, N., Bali, R., Gieniusz, R., Mamica, S., Gollwitzer, J., Schneider, T., Lenz, K., Potzger, K., Lindner, J., Krawczyk, M., Fassbender, J. & Maziewski, A. (2015*a*). *Phys. Rev. B*, **92**, 144429–1–7.
Tahir, N., Gieniusz, R., Maziewski, A., Bali, R., Potzger, K., Lindner, J. & Fassbender, J. (2015*b*). *Opt. Express*, **23**, 16577.
Trammell, G. T. (1962). *Phys. Rev.* **126**, 1045–1054.
Trammell, G. T. & Hannon, J. P. (1978). *Phys. Rev. B*, **18**, 165–172.
Voronina, E. V., Arzhnikov, A. K., Chumakov, A. I., Chistyakova, N. I., Ivanova, A. G., Pyataev, A. V. & Korolev, A. V. (2018). *Adv.Condensed Matter Phys.* **2018**, 5781873.
Yelsukov, E. P., Voronina, E. V. & Barinov, V. A. (1992). *J. Magn. Magn. Mater.* **115**, 271–280.
Ziegler, J. F., Ziegler, M. D. & Biersack, J. P. (2010). *Nucl. Instrum. Methods Phys. Res. B*, **268**, 1818.